



Contents lists available at ScienceDirect



Catalysis Today

journal homepage: www.elsevier.com/locate/cattod

Highly efficient Cu-based catalysts via hydrotalcite-like precursors for CO₂ hydrogenation to methanol

Shuo Xiao ^{a,b}, Yanfei Zhang ^{a,b}, Peng Gao ^{a,*}, Liangshu Zhong ^a, Xiaopeng Li ^a, Zhongzheng Zhang ^a, Hui Wang ^{a,**}, Wei Wei ^{a,c}, Yuhua Sun ^{a,c}

^a CAS Key Lab of Low-Carbon Conversion Science and Engineering, Shanghai Advanced Research Institute, Chinese Academy of Sciences, No.99 Haik Road, Zhangjiang Hi-Tech Park, Shanghai 201210, China

^b School of Environmental and Chemical Engineering, Shanghai University, Shanghai 200444, China

^c School of physical Science and Technology, ShanghaiTech University, Shanghai 201210, China

ARTICLE INFO

Article history:

Received 11 September 2015

Received in revised form 1 January 2016

Accepted 1 February 2016

Available online xxx

Keywords:

Carbon dioxide hydrogenation

Methanol synthesis

Hydrotalcite-like structure

Copper particle size

Copper-based catalyst

ABSTRACT

A series of Cu-Zn-Al-Zr precursor materials are prepared by coprecipitation at different pH values (6.0–11.0) and treated under hydrothermal condition. Zincian malachite is formed as the main phase at the low pH of 6.0 and 7.0, and is replaced by hydrotalcite-like phases with increasing the pH. After calcination and reduction of precursors, Cu/ZnO/Al₂O₃/ZrO₂ catalysts are obtained and tested for methanol synthesis from CO₂ hydrogenation at the reaction temperature of 463 K. With increasing pH, the Cu particle size first increases until pH 9.0 and then decreases. Compared with the sample resulting from well-crystallized zincian malachite (pH 7.0), the catalysts derived from phase-pure hydrotalcite-like precursors (pH ≥ 9.0) exhibit lower BET specific surface area and lower specific Cu surface area. In addition, due to the smaller of Cu particle size and the stronger interaction among Cu and ZnO, the catalytic activity for the Cu/ZnO/Al₂O₃/ZrO₂ catalysts via the hydrotalcite-like precursors is higher than that for the catalysts derived from zincian malachite precursors at low reaction temperature. A maximum CH₃OH yield of 0.087 g gcat⁻¹ h⁻¹ with the CO₂ conversion of 10.7% and the CH₃OH selectivity of 81.8% at 463 K and 5.0 MPa is obtained over the Cu/ZnO/Al₂O₃/ZrO₂ catalyst prepared at pH 9.0.

© 2016 Elsevier B.V. All rights reserved.

1. Introduction

Catalytic conversion of CO₂ to useful chemicals and fuels is a promising route that may offer a solution to the issues of greenhouse gas control and fossil fuel substitution. Methanol is a common feedstock for several important chemicals and can be used as a fuel additive or clean fuel. It can also be converted to high-octane gasoline, aromatics, ethylene, propylene as well as other useful petrochemicals which now are derived from crude oil [1,2]. In this context, hydrogenation of CO₂ to methanol has attracted much attention from both industry and academia.

The Cu/ZnO/Al₂O₃ catalyst, used for methanol synthesis from syngas in industry, is also widely investigated for CO₂ hydrogenation to methanol [3–7]. However, the low activity of industrial Cu/ZnO/Al₂O₃ catalysts creates major barriers toward direct

application to CO₂ hydrogenation. Especially, at low reaction temperature, their behavior is the deactivation of Cu-based catalysts due to the high activation energy of hydrogen dissociation [8,9]. It has been suggested that the high activity for CO₂ hydrogenation was generated by the presence of surface defects of metallic Cu surface which could reduce the activation energy of hydrogen dissociation [10,11]. In addition, rich surface defects can be achieved by decreasing the size of Cu nanoparticles with a simultaneous high dispersion. Great efforts have been made to decrease the copper particle size for Cu/ZnO-based catalysts by addition of various promoters such as Zr, Ti, Ga, Y, Ce and B [5,12–14]. The influences of synthesis conditions and pre-treatment process on the copper crystallite size of Cu/ZnO-based catalysts were also investigated [15–18].

With the use of Cu-Zn-Al hydrotalcite-like (HTl) precursors, small Cu clusters are generated as the active sites for methanol synthesis from syngas or CO₂ hydrogenation [19–22]. The composite oxides derived from hydrotalcite-like compounds (HTlcs) possess homogeneous dispersion of metal at an atomic level, enhanced synergistic effects among different elements, strong basic properties

* Corresponding author. Fax: +86 21 20608003.

** Corresponding author.

E-mail addresses: gaopeng@sari.ac.cn (P. Gao), wanghh@sari.ac.cn (H. Wang).

and high stability against sintering [23–25]. Moreover, by virtue of the wide versatility of HTIcs composition and architecture, metal nanoparticles with high dispersion, high density, and good thermal stability for catalysis can be fabricated via reduction of HTI precursors [26]. In our previous work, we presented Cu/ZnO/Al₂O₃/ZrO₂ catalysts with promising catalytic performance in the CO₂ hydrogenation to methanol obtained from HTI precursors [19,27,28], and found that the catalytic activity decreased with significant decrease of the yield of HTI phase in precursors [19]. HTIcs are conventionally synthesized through coprecipitation methods. However, such process suffers from a product with a low crystallinity. Especially, much amorphous phases were formed with the introduction of large radius of metal cations (such as Y³⁺, Ce³⁺ and Zr⁴⁺) into HTI structures [14,19]. The product crystallinity can be affected by various reaction parameters (pH, temperature, concentration and rate of added solutions, and the aging temperature and time) and/or post-synthesis operations (for example, aging of the precipitate) [29]. A substantial improvement of the product crystallinity can be achieved by hydrothermal treatment and the hydrothermal treatment was applied to improve the crystallinity of many kinds of HTIcs [29–31].

Furthermore, the typical hydroxy carbonate precursor phases for industrial Cu/ZnO/Al₂O₃ catalysts are zincian malachite, aurichalcite, or a phase mixture of zincian malachite and aurichalcite [32]. The crystal phase of the precursor was mainly depended on the metal composition, for example, high Al content was favourable for the formation of HTI phase [28] and zincian malachite or aurichalcite phases were formed as a main phase at the low Al content [17]. Al₂O₃ has been pointed out to work as the promoter to increase the stability and the activity [33], thus the Al content will affect the catalytic performance for CO₂ hydrogenation to methanol. So far, few comparative studies on the influences of different precursors with the same metal composition on the catalyst activity exist.

In the present work, a series of Cu-Zn-Al-Zr precursors (Cu²⁺:Zn²⁺:Al³⁺:Zr⁴⁺ = 2:1:1.2:0.1) were synthesized by coprecipitation method at different pH values (6.0–11.0) and treated under hydrothermal conditions at 293 K. The Cu/ZnO/Al₂O₃/ZrO₂ catalysts were then obtained by calcination and reduction of precursors and tested for methanol synthesis from CO₂ hydrogenation at 463 K. The main focus is to study the effect of pH conditions on physicochemical properties of precursor materials, related mixed oxides, and reduced samples. In addition, the effects of pH of preparation on the catalytic performance were investigated for the structure–activity relationship. This work also allowed us to investigate how different precursors can affect the catalytic activity for CO₂ hydrogenation to methanol.

2. Experimental

2.1. Preparation of catalysts

Cu/ZnO/Al₂O₃/ZrO₂ catalysts with Cu²⁺:Zn²⁺:Al³⁺:Zr⁴⁺ = 2:1:1.2:0.1 were synthesized by a co-precipitation method at 293 K. Typically, two aqueous solutions, a solution of the metal nitrates and a mixed solution of NaOH and Na₂CO₃ precipitant, were added dropwise to 200 mL of deionized water under vigorous stirring. The mixed solution was conducted at pH range of 6.0–11.0. The product was then transferred into the Teflon coated stainless steel autoclave for hydrothermal treatment at 373 K for 16 h under autogenous water vapor pressure. After the hydrothermal treatment, the precipitate was filtered and washed with deionized water. The filter cakes were dried overnight at 353 K. The samples were calcined in air at 773 K for 5 h, and the obtained samples were crushed and sieved to particles in the

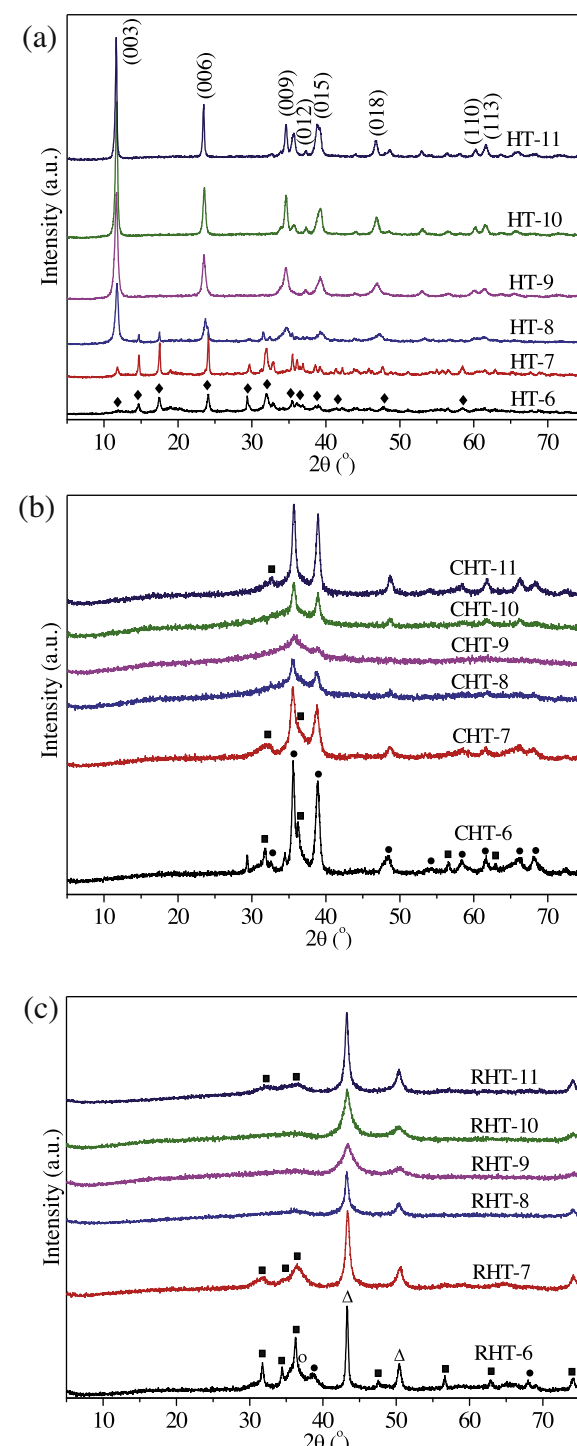


Fig. 1. XRD patterns of (a) uncalcined materials, (b) calcined samples and (c) reduced Cu/ZnO/Al₂O₃/ZrO₂ catalysts prepared at various pH conditions. (♦) Zincian malachite, (Cu,Zn)₂(OH)₂CO₃; (Δ) Cu; (○) Cu₂O; (●) CuO; (■) ZnO.

range of 40–60 mesh. The as-obtained precursors with different pH were denoted as HT-*n* (*n* is pH during precipitation), and the corresponding calcined and reduced samples were denoted as CHT-*n* and RHT-*n*, respectively.

2.2. Characterization of catalysts

The chemical composition of the calcined samples was determined by X-ray fluorescence (XRF) spectroscopy (PW2404 X-ray wavelength dispersive spectrometer).

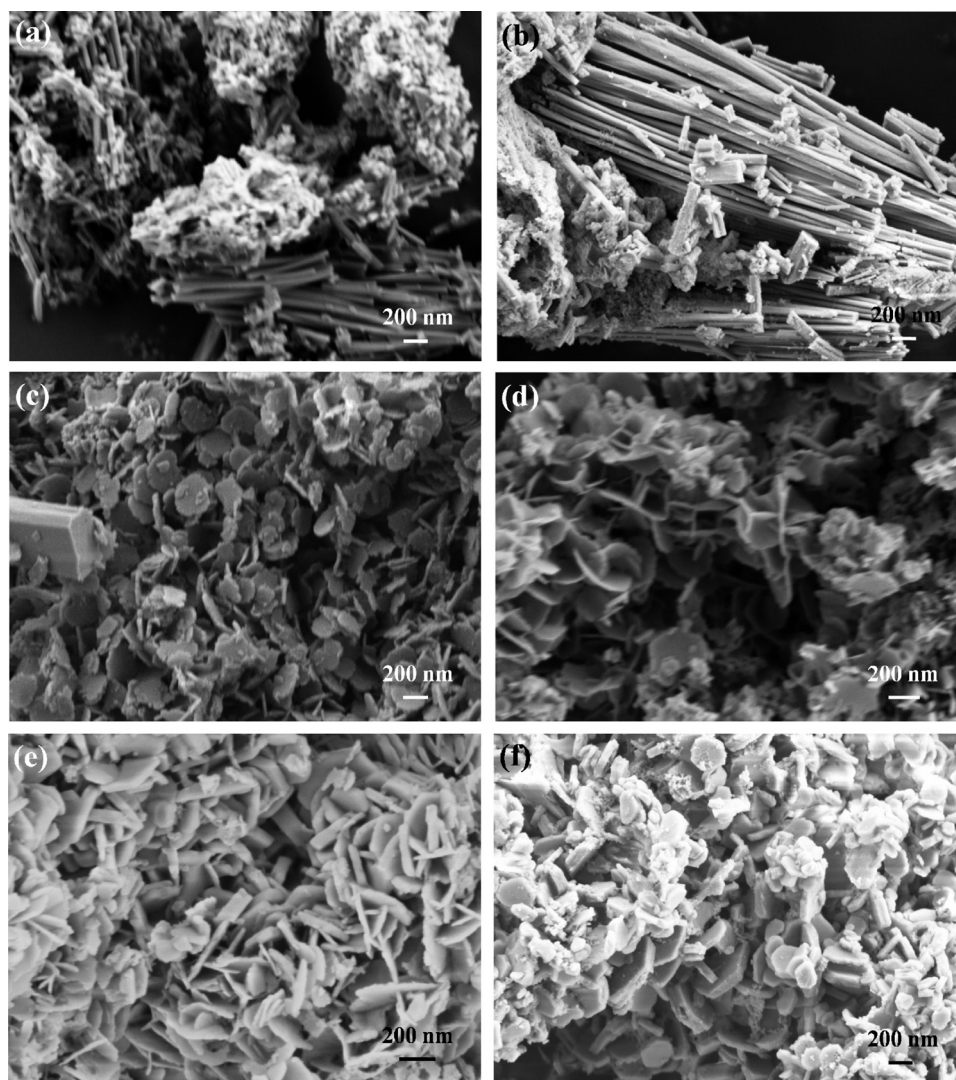


Fig. 2. SEM images of Cu–Zn–Al–Zr precursor materials (a) HT-6, (b) HT-7, (c) HT-8, (d) HT-9, (e) HT-10, (f) HT-11.

The surface area of samples was determined by N_2 adsorption–desorption at liquid nitrogen temperature 77.30 K, using a TriStar II 3020 instrument. Sample degassing was carried out at 473 K prior to acquire the adsorption isotherm. BET isotherm and BJH model were used to obtain specific surface area and pore volume, respectively.

Powder X-ray diffraction (XRD) patterns were recorded on a Rigaku Ultima 4 X-ray diffractometer with Cu $K\alpha$ radiation in the range of $5^\circ < 2\theta < 75^\circ$.

The morphology of the samples was investigated using a ZEISS SUPRA 55 scanning electron microscope (SEM) with an accelerating voltage of 2.0 kV.

Thermogravimetric mass spectrometry (TG–MS) analysis was performed by using a STA449-QMS thermal analyzer. Samples were heated up to 1023 K with linear temperature program at a heating rate of 10 K min^{-1} in continuous flow of synthetic air (30 mL min^{-1}).

Transmission electron microscope (TEM) and high resolution transmission electron microscope (HRTEM) were performed on a JEM 2100 transmission electron microscope with a field emission gun operating at 200 kV to investigate the dimensions and the structural details of the reduced catalysts.

The exposed Cu surface area (S_{Cu}) was determined by dissociative N_2O adsorption and carried out on Micromeritics AutoChem 2920 instrument using the procedure described in our previous

work [14]. Before measurements the catalysts (0.1 g) were reduced at 573 K in 5% H_2 /Ar mixture (30 mL min^{-1}) for 2 h. The reduced samples cooled to 303 K and isothermally purged with Ar for 30 min. Then, the sample was exposed to N_2O (85 mL min^{-1}) for 1 h to ensure complete oxidation of surface metallic copper. Finally, a pulse of pure H_2 was passed over the catalyst at 573 K and the surface Cu_2O was reduced in the pulse of pure H_2 . S_{Cu} was calculated from the amount of hydrogen consumption (n_{H_2}). In addition, the dispersion of Cu (D_{Cu}) was calculated by Eq. (1).

$$D_{\text{Cu}} = \frac{(2n_{H_2} \times M_{\text{Cu}}/W) \times 100\%}{X} \times 100\% \quad (1)$$

where n_{H_2} was molar number of consumed H_2 . D_{Cu} was the dispersion of Cu, M_{Cu} was relative atomic mass ($63.546 \text{ g mol}^{-1}$), W was the weight of the catalyst, and X was the composition of Cu (wt.%) determined by X-ray fluorescence spectroscopy.

X-ray photoelectron spectroscopy (XPS) and Auger electron spectroscopy (XAES) were performed over a Quantum 2000 Scanning ESCA Microprobe instrument equipped with Al $K\alpha$ radiation (12 kV , 4 mA , $h\nu = 1486.6 \text{ eV}$) under ultrahigh vacuum (10^{-7} Pa). Prior to each test, the calcined sample was reduced in pure hydrogen at 553 K for 6 h, and XPS measurements were recorded with the exclusion of air contact after reduction. The binding energies

were calibrated internally by adventitious carbon deposit C (1s) with $E_b = 284.8$ eV (accuracy within ± 0.1 eV).

Temperature program reduction (TPR) was conducted in a U-tube quartz reactor on a Micromeritics ChemiSorb 2920 with a thermal conductivity detector (TCD). 50 mg of sample placed in a U-tube quartz reactor was first degassed under flowing argon (30 mL min^{-1}) at 423 K for 1 h and cooled down to room temperature. Then the sample was reduced at a rate of 5 K min^{-1} up to 873 K in a flow of $5\% \text{H}_2/\text{Ar}$ (30 mL min^{-1}) mixture.

2.3. Evaluation of catalysts

Activity measurements in the hydrogenation of CO_2 were carried out in a fixed-bed reactor. Catalyst (1.5 mL, 40–60 mesh) diluted with 1.5 mL quartz sand (40–60 mesh) was placed in a stainless steel tube reactor. Prior to reaction, the catalyst was reduced in pure H_2 at a flow-rate of 80 mL min^{-1} under atmospheric pressure. The reduction temperature was programmed to increase from room temperature to 553 K and maintained at 553 K for 6 h. The reactor was then cooled to room temperature. After reduction, the activities of the catalyst samples in CO_2 hydrogenation process were determined under reaction conditions of 463 K, 5.0 MPa, $\text{H}_2/\text{CO}_2/\text{N}_2 = 73/24/3$, $\text{GHSV} = 4000 \text{ h}^{-1}$. The products were quantitatively analyzed using a Shimadzu GC-2010C gas chromatograph equipped with a thermal conductivity detector (TCD, TDX-01 column) for gas of H_2 , N_2 , CO , CH_4 and CO_2 , and Porapak-Q for liquid of H_2O and CH_3OH . The CO_2 conversion and the carbon-based selectivity for CH_3OH and CO were calculated by an internal normalization method. The yield of CH_3OH , which gave the amounts of CH_3OH produced per gram catalyst per hour, was defined as Eq. (2):

$$Y(\text{CH}_3\text{OH}) = \frac{W_T \times X(\text{CH}_3\text{OH})}{t \times m} \quad (2)$$

where W_T was the total weight of CH_3OH and H_2O product (g); $X(\text{CH}_3\text{OH})$ was the mass fraction of CH_3OH ; t was the reaction time (h); m was the weight of catalyst (g).

3. Results and discussion

3.1. Textural and structural properties of the precursor materials

The powder XRD patterns of Cu-Zn-Al-Zr precursors at different pH conditions are depicted in Fig. 1a. The zincian malachite [rosasite, $(\text{Cu},\text{Zn})_2(\text{OH})_2\text{CO}_3$] was formed as a main phase at the low pH of 6.0 and 7.0, and was replaced by hydrotalcite-like (HTl) phases with increasing the pH. For HT-8, both zincian malachite and HTl phases can be detected, and HTl phase was the main phase. Hydrotalcite alone was selectively produced at the high pH, above 8.0. The patterns of HT-9, HT-10, and HT-11 samples exhibited typical reflections of HTl structure: sharp and symmetrical peaks for (0 0 3), (0 0 6), (1 1 0) and (1 1 3), and broad and asymmetrical for (0 0 9), (0 1 5) and (0 1 8), respectively [34,35]. In addition, the narrow peaks indicated that hydrotalcites were present as a well-defined crystalline phase, and the well-defined (1 1 0) and (1 1 3) diffraction peaks were also observed at 60° and 61° , suggesting a homogeneous dispersion of various cations in the hydroxide layers [34]. As pH increases, from 8.0 to 11.0, the intensity of the reflections increased and the line width decreased, corresponding to an increase in crystallinity.

The fibrous morphology of HT-6 and HT-7 precursors was observed by using scanning electron microscopy (SEM), as presented in Fig. 2a and b, respectively, and the fibers size for HT-7 ($1\text{--}3 \mu\text{m}$) was much larger than that for HT-6 ($0.5\text{--}1.3 \mu\text{m}$). As shown in Fig. 2c–f, the expected platelet-like morphology of hydrotalcite-like compounds (HTlc's) can be observed for HT-8,

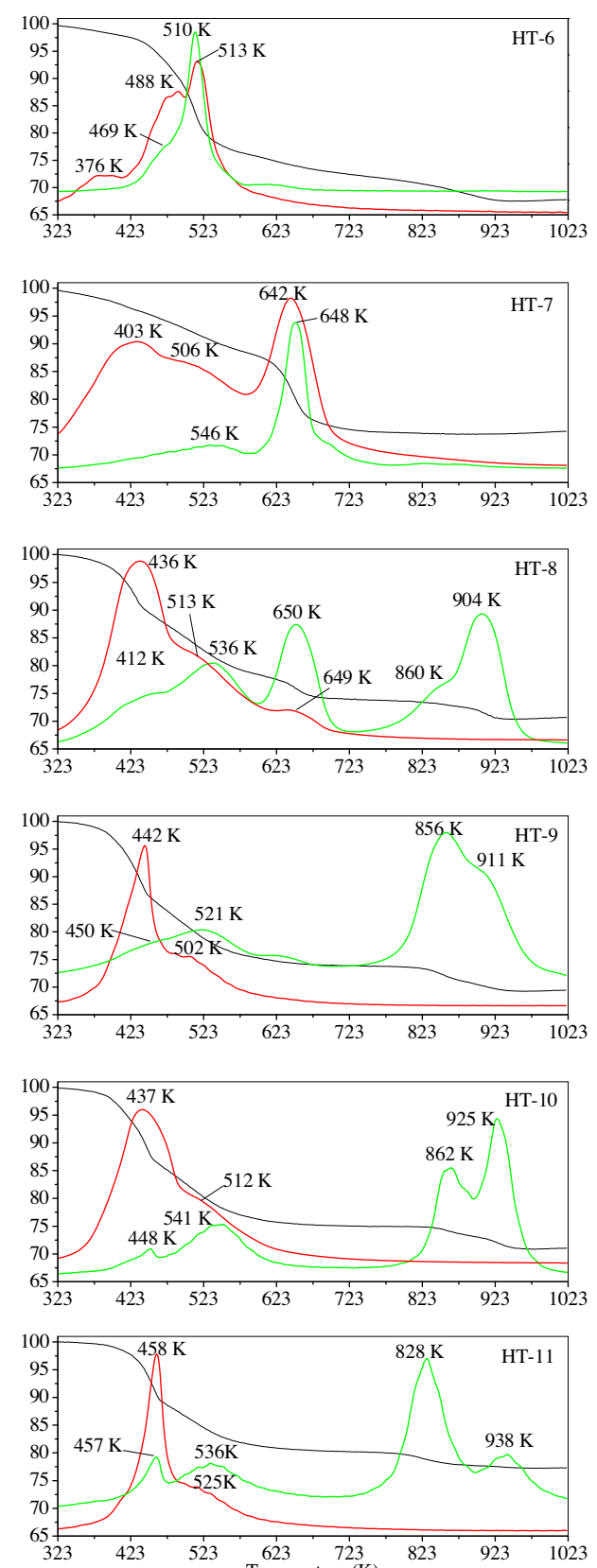


Fig. 3. Thermogravimetry mass spectrometry (TG-MS) profiles of Cu-Zn-Al-Zr precursors in synthetic air. (red line) H_2O , (green line) CO_2 , (black line) mass loss (%). For interpretation of the references to color in this figure legend, the reader is referred to the web version of this article.

HT-9, HT-10 and HT-11 samples. In addition, the platelets were well-developed and intercrossed with each other, and most of the edges were rounded at low pH. With increasing pH from 8.0 to 11.0, both the diameters and thicknesses of platelets increased significantly and the dispersion of platelets decreased. For the HT-8 precursor, minor amounts of fibers with thick dimension can also be found, which is consistent with the XRD result.

Calcination of the precursors was simulated by thermogravimetric (TG) measurements in synthetic air together with the evolved H_2O and CO_2 curves detected upon heating by using mass spectrometry (MS), and the resulting curves for all samples are shown in Fig. 3. HT-6 and HT-7 samples exhibited the same phase composition and more X-ray amorphous phases existed in HT-6, as judged by the diffraction patterns. In the whole temperature range, the behavior was quite similar and three H_2O emission peaks and two peaks belongs to CO_2 can be observed, while all peaks shifted to lower temperatures remarkably as pH decreases, from 7.0 to 6.0, which revealed the much lower thermal stability of HT-6 and the structural differences between the two precursors. In addition, the dehydroxylation and decarboxylation of the zincian malachite (HT-6 and HT-7) were completed around 773 K. With further increase of pH from 8.0 to 11.0, the typical 3-step decomposition of HTIcs was observed [21,28]. First, the peaks around 450 K can be attributed to the elimination of physically adsorbed H_2O and CO_2 molecules and evaporation of interlamellar water molecules. The second weight loss at 473–773 K was ascribed to dehydroxylation of the HTI layer and loss of carbonate of the interlayer space. For HT-8 sample, the second weight loss peak can be also due to the decomposition of zincian malachite phase. Moreover, CO_2 formation above 823 K was observed, which can be assigned to the stabilizing "high temperature carbonate" formed during the former steps of the thermal decomposition of the HTI structure. This carbonate species, which possessed strong interfacial interaction and stable grain boundaries, were trapped between segregating CuO particles and other metal oxides during calcination of precursors [21,36].

3.2. Textural and structural properties of the calcined samples

The results of the elemental analysis of the calcined samples are included in Table 1. The $\text{Cu}^{2+}:\text{Zn}^{2+}:\text{Al}^{3+}:\text{Zr}^{4+}$ atomic ratios determined from X-ray fluorescence spectroscopy (XRF) were in close agreement, within experimental errors, with the nominal compositions (2:1:1.2:0.1) taken for the catalysts preparations, indicating the complete precipitation of the metallic nitrates for all samples, except for CHT-6. Only at the acidic condition (pH 6.0), the determined ratio of CHT-6 was significantly deviated from the nominal data, for example, with lower $\text{Al}^{3+}/\text{Zn}^{2+}$ and $\text{Zr}^{4+}/\text{Zn}^{2+}$ ratios and a higher $\text{Cu}^{2+}/\text{Zn}^{2+}$ atomic ratio, suggesting that more copper nitrates were precipitated in the solution compared to other metallic nitrates at pH 6.0. XRD patterns of the calcined samples are shown in Fig. 1b. The peaks in CHT-6 XRD pattern were assigned to CuO and ZnO with good crystalline. The crystallinity of the calcined samples decreased significantly with increasing pH from 6.0 to 9.0, while the intensity of the reflections increased remarkably with further increase of pH. When pH ≥ 8.0, only the diffraction peaks belonging to a CuO phase were detected and there were no peaks that can be attributed to ZnO . In addition, the CHT-9 pattern showed low signal-noise ratio and the weakest peak intensity, and the larger half-peak width indicated the relatively small crystalline size of CuO compared to other calcined samples. The CuO crystallite size (d_{CuO}) was also calculated by the Scherrer equation, and d_{CuO} decreased significantly with increasing pH until pH 9.0 and then increased (Table 1).

SEM images of the calcined samples are shown in Fig. 4. The zincian malachite fibers prepared at pH 6.0 transformed into the spherically shaped and compact particles (Fig. 5a) during

calcination at 773 K. It can be seen that the other samples upon thermal decomposition maintained morphology similar to that of the precursors. For CHT-7, the nano-structuring of homogeneous particles and the generation of pores can be found in Fig. 5b. The calcined CHT-8, CHT-9, CHT-10 and CHT-11 samples were composed of platelet-like particles, suggesting that the derived oxides remained the morphological characteristic of HTI precursors.

The textural properties of CHT-*n* samples prepared at different pH values are summarized in Table 1. The BET specific surface area (S_{BET}) of CHT-6 was much lower than those of other samples due to the formation of compact particles during calcination as a result of the much lower thermal stability of the HT-6 precursor. CHT-7 exhibited the highest S_{BET} , and it decreased with increasing pH, indicating the metal oxides derived from well-crystallized zincian malachite possessed higher S_{BET} compared to HTI precursors. For the samples via phase-pure HTIcs, the decline of S_{BET} with increasing pH can be ascribed to the decrease of the dispersion of platelets.

3.3. Textural and structural properties of the reduced samples

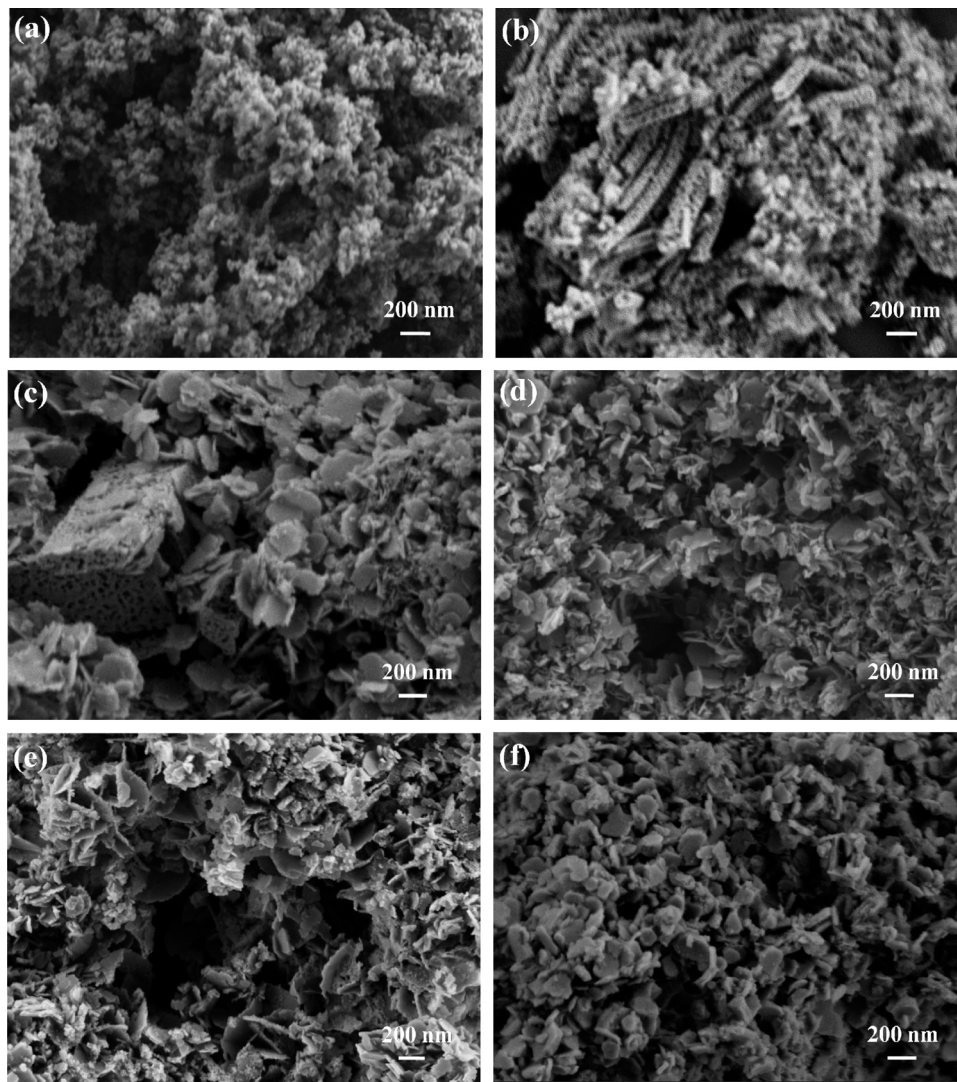
XRD patterns obtained for reduced and passivated CHT-*n* samples are displayed in Fig. 1c. The calcined samples reduced in a 10% H_2/Ar flow at 553 K for 6 h, and passivation was carried out at 298 K in a flow of 1% O_2/Ar for 60 min. As shown in Fig. 1c, the XRD diffraction peaks ($2\theta = 35.6^\circ$ and 38.8°) of CuO disappeared in all catalysts except of RHT-6, while the peaks ($2\theta = 43.2^\circ, 50.2^\circ$, and 74.1°) attributed to metallic Cu emerged. For RHT-6, apart from metallic Cu, the diffraction peaks of CuO can be still observed and poorly crystallized Cu_2O can also be found after reduction at 553 K, indicating that the amount of reducible copper species for the RHT-6 sample was much lower than that for the other samples below 553 K. The intensity of diffraction peaks of ZnO decreased markedly with increase of pH, and the peaks due to ZnO cannot be observed when pH ≥ 8.0, except for the sample prepared at pH 11.0. Compared with RHT-6 and RHT-7, rather weak peaks due to a poorly crystallized ZnO phase were detectable in the XRD patterns of RHT-11. These results revealed that the ZnO dispersions in catalysts via HTI precursors were better than those in samples derived from zincian malachite. In addition, the Cu crystallite size (d_{Cu}) calculated by the Scherrer equation decreased markedly with increasing pH, while the average Cu particle size increased when pH > 9.0, and the minimum d_{Cu} was 6.5 nm for RHT-9 (Table 1). After reduction of CHT-*n* catalysts, d_{Cu} was larger than corresponding d_{CuO} for RHT-6 and RHT-7 derived from zincian malachite, suggesting that sintering of copper particles occurred upon heat treatment. Compared with reduced samples derived from zincian malachite, the d_{Cu} for the samples via HTI precursors was much lower, especially for RHT-9 (only 6.5 nm). These results indicated that the HTI structure can hinder the growth of Cu particle size during the calcination and reduction.

The transmission electron microscopy (TEM) and high resolution transmission electron microscopy (HRTEM) images illustrate the typical microstructure of the reduced CHT-*n* catalysts. The RHT-7 sample comprised the much compact particles (Fig. 5a). After the reduction of CHT-9 and CHT-11 at 553 K for 6 h, the samples still maintained the overall plate-like morphology (Fig. 5b and c), while abundant dispersed small dots were observed throughout the plates. On platelets of RHT-9, spherically shaped and well crystalline of Cu could be noticed from HRTEM images and no indication for individual separated oxide particles were found (Fig. 5d). The average diameter of Cu particles for RHT-9 was around 5–9 nm, in agreement with the result from XRD analysis (Table 1). In addition, the Cu particles were partly embedded in the remaining metal oxide matrix resulting in close interfacial contact of Cu particles and continuous Cu depleted oxide. Therefore, the extrapolation of the

Table 1

Structure and composition of calcined samples prepared at different pH.

Sample	$\text{Cu}^{2+}:\text{Zn}^{2+}:\text{Al}^{3+}:\text{Zr}^{4+}$ atomic ratio ^a	Crystallite sizes (nm) ^b		S_{BET} ($\text{m}^2 \text{g}^{-1}$)	S_{Cu}^c ($\text{m}^2 \text{g}^{-1}$)	D_{Cu}^c (%)
		CuO	Cu			
CHT-6	2.72:1:0.84:0.06	23.9	28.0	28	10.1	2.74
CHT-7	2.25:1:1.12:0.09	14.0	14.6	112	29.2	8.85
CHT-8	2.21:1:1.24:0.10	13.1	11.7	79	21.9	7.00
CHT-9	2.28:1:1.19:0.08	8.8	6.5	68	19.4	6.07
CHT-10	2.12:1:1.14:0.08	12.2	8.1	59	16.9	5.45
CHT-11	2.29:1:1.12:0.08	16.9	13.8	46	16.6	5.16

^a Determined by X-ray fluorescence spectroscopy.^b Determined from full width at half maxima of CuO (1 1 1) or Cu (1 1 1) XRD peak.^c Calculated from N_2O dissociative adsorption.**Fig. 4.** SEM images of calcined samples (a) CHT-6, (b) CHT-7, (c) CHT-8, (d) CHT-9, (e) CHT-10, (f) CHT-11.

interaction among Cu and ZnO for RHT-9 was stronger than that for RHT-7. For the RHT-11, apart from Cu particles, the separated ZnO particles were formed according to the XRD analysis, thus more agglomerated particles on the platelets could be observed (Fig. 5c).

The reactive N_2O adsorption on reduced samples (Table 1) was to determine the exposed copper surface area (S_{Cu}) and dispersion of copper (D_{Cu}). It was found that the variations of S_{Cu} and D_{Cu} were consistent with the trend of the S_{BET} . Compared with the RHT-7 derived from well-crystallized zincian malachite, S_{Cu} for the catalysts (RHT-9, RHT-10 and RHT-11) via phase-pure HTIcs was

much lower. The Cu particles were embedded in oxidic matrix for RHT-9, while were well-separated from ZnO for RHT-7 as illustrated by TEM and XRD, thus the lower Cu surface area can be accessible to the gas phase for the sample resulting from the HTI precursor.

3.4. XPS investigations on reduced samples

XPS analysis was performed to determine the surface chemical states and compositions of reduced RHT-n catalysts. As shown in Fig. 6a, XPS spectrum of RHT-6 exhibited broad peaks for $\text{Cu}_{2\text{p}3/2}$

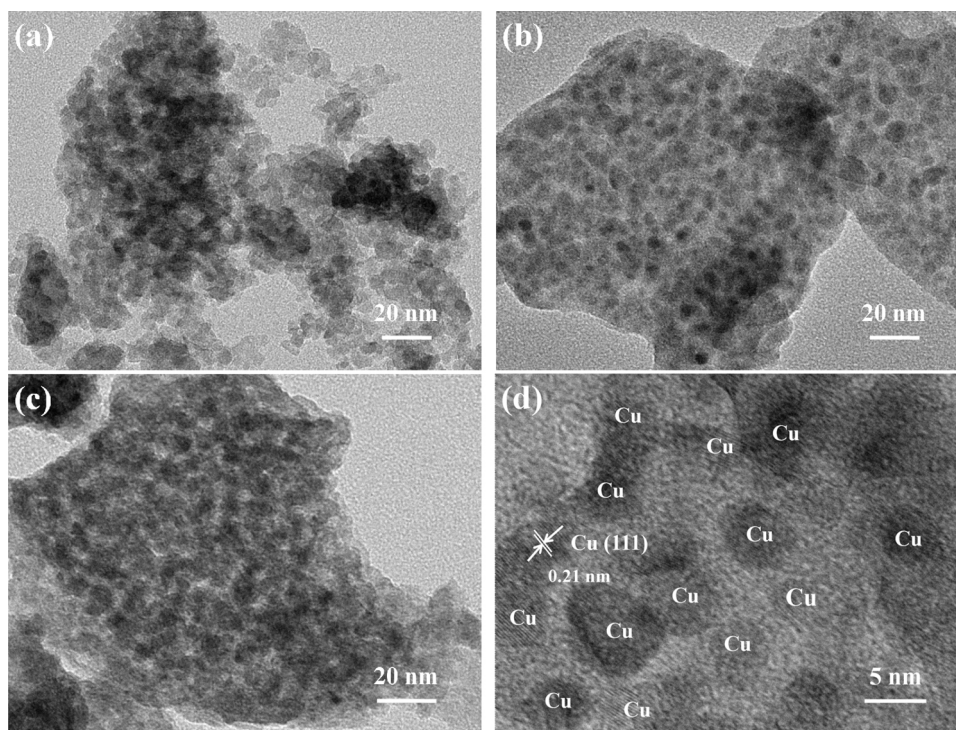


Fig. 5. TEM images of RHT-*n* samples after reduction at 553 K for 6 h: (a) RHT-7, (b) RHT-9, (c) RHT-11, and (d) HRTEM images of the RHT-9 sample.

at 933 eV and 942 eV as parent and satellite peak, respectively, and XPS peaks were found at around 953 eV and 962 eV for Cu2p_{1/2} core electrons and satellite excitations. The emergence of the satellite structure indicated that some Cu²⁺ species were still present on the surface of RHT-6 after reduction at 553 K for 6 h [37]. For other reduced samples, the spectra consisted of two peaks at around 932 and 952 eV which were mainly ascribed to Cu 2p_{3/2} and Cu2p_{1/2} peaks of Cu⁰, respectively [38]. The absence of satellite peaks around 942 and 962 eV revealed that the Cu²⁺ species for the samples prepared at pH ≥ 7.0 were reduced completely after reduction at 553 K. In addition, the Zn 2p_{3/2} peak at 1020.9–1021.4 eV can be attributed to the Zn²⁺ species on the catalyst surface (Fig. 6b).

The binding energies (BE) of Cu 2p_{3/2}, Zn 2p_{3/2} and Al 2p bands and surface compositions of the RHT-*n* catalysts are listed in Table 2. It was found that both the BE of Cu 2p_{3/2} and Zn 2p_{3/2} bands increased gradually with increasing pH. Obviously, these BE for the catalysts (pH ≥ 8.0) mainly derived from HTI precursors were higher than those for the RHT-7 sample resulting from zincian malachite. Additionally, the Al 2p core-level was located at BE around 74.0 eV for all the reduced samples and the BE of Zr 3d_{3/2} and Zr 3d_{5/2} changed slightly with increase of pH (Fig. 6c). These results illustrated that there existed interaction between Cu and ZnO and this interaction was weakened at low pH of 7.0, which can be ascribed to lower dispersion of ZnO. Relative surface concentrations of metal the catalysts, as determined by XPS, are compared in Table 2 with the bulk compositions measured by XRF. For RHT-6, the surface contents of all metals were similar to the bulk compositions. However, the surface was significantly depleted of Cu for other reduced samples, whereas Zn was enriched. In addition, the Zr accumulated preferentially on the surface (an increase of three to five times compared to the data measured by XRF). It was also clearly seen that the surface Cu content and the surface Cu/Zn ratio raised first and then decreased with increasing pH from 7.0 to 11.0 and the maximums were found for RHT-9.

3.5. The reducibility of Cu/ZnO/Al₂O₃/ZrO₂ catalysts

In order to obtain a better understanding of the reduction process, CHT-*n* samples were carefully analyzed by using TPR measurements (Fig. 7). The CHT-6 and CHT-7 samples derived from zincian malachite presented one peak of hydrogen consumption. The reduction peak of CHT-6 was around 575 K, while the profiles of other samples showed no H₂ consumptions at temperatures above 565 K, which suggested that the reducibility of CHT-6 was much lower than those of other calcined samples, is consistent with the XRD and XPS results. The CHT-8, CHT-9 and CHT-10 samples via HTI precursors possessed the bimodal TPR profiles. Kühl et al. [21] suggested that the reduction of the Cu/ZnO/Al₂O₃ catalyst resulting from a Cu-Zn-Al hydroxide-like compound proceeded in two steps through a kinetically stabilized Cu⁺ intermediate due to the strong interaction between Cu²⁺ species and Zn-Al-oxide. Moreover, many studies claimed that the reduction of CuO to metallic Cu passed through an intermediate Cu⁺ species [33,37]. Therefore, this can explain the pronounced shoulder of the TPR signal for CHT-8, CHT-9 and CHT-10. In addition, the position of the second reduction peak for CHT-9 was much lower than those for CHT-8 and CHT-10, which can be attributed to the smaller CuO particles. CHT-11 exhibited three reduction peaks and the first peak centered at 489 K which was closed to the position of the reduction peak for CHT-7. According to the XRD and TEM analysis of CHT-11, a part of CuO particles were well-separated from ZnO for CHT-11, therefore, the reduction behavior of these CuO particles was similar to that of CHT-7.

3.6. Catalytic performance

Activity data of various Cu/ZnO/Al₂O₃/ZrO₂ catalysts in methanol synthesis from CO₂ hydrogenation are summarized in Table 3. Methanol and CO are the only carbon-containing products at low reaction temperature (463 K). The catalytic activity for Cu/ZnO/Al₂O₃/ZrO₂ catalysts via HTI precursors was better than

Table 2XPS results for the reduced Cu/ZnO/Al₂O₃/ZrO₂ catalysts prepared at different pH.

Sample	Binding energy (eV)			Relative surface concentration of metal (at.%) ^a				Cu/Zn
	Cu 2p _{3/2}	Zn 2p _{3/2}	Al 2p	Cu	Zn	Al	Zr	
RHT-6	933.1	1021.3	74.5	52.3 (58.9)	24.9 (21.6)	18.4 (18.1)	4.3 (1.3)	2.10
RHT-7	932.0	1021.3	74.3	34.9 (50.5)	35.0 (22.4)	24.3 (25.1)	5.8 (2.0)	1.00
RHT-8	932.3	1021.7	74.3	38.1 (48.6)	37.3 (21.9)	17.6 (27.2)	7.0 (2.3)	1.02
RHT-9	932.4	1021.8	74.4	39.6 (50.2)	31.5 (22.0)	22.8 (26.1)	6.2 (1.7)	1.26
RHT-10	932.4	1021.8	74.4	29.4 (48.9)	39.1 (23.0)	23.0 (26.3)	8.5 (1.8)	0.75
RHT-11	932.3	1021.6	74.3	28.3 (51.2)	44.1 (22.4)	21.4 (24.7)	6.2 (1.7)	0.64

^a Values in parentheses are concentration normalized to the total metal content measured by XRF.

that for the catalysts derived from zincian malachite precursors. In addition, both CO₂ conversion and CH₃OH yield took on a volcanic trend with increasing pH. The CO₂ conversion over RHT-6 was much lower than those over other catalysts. Most researchers proposed that the Cu⁰ species were the predominant active sites for methanol synthesis from CO₂ hydrogenation [10,38–40]. As discussed above, the CHT-6 sample was not reduced completely at 553 K and three kinds of copper species (Cu, Cu⁺, Cu²⁺) were present after reduction, which might result in the much lower activity for RHT-6. A maximum CO₂ conversion of 10.7% with the CH₃OH yield of 0.087 g gcat⁻¹ h⁻¹ was obtained over the catalyst prepared at pH 9.0. Under the similar reaction conditions, the CO₂ conversions for other types of the Cu/ZnO-based catalysts were around 6% [41,42]. Therefore, the Cu/ZnO/Al₂O₃/ZrO₂ catalysts via HTIcs exhibited excellent performance for CO₂ hydrogenation. For all catalysts, except for RHT-6, the CH₃OH selectivity was very high, above 80%, because the low temperature was favorable for the reaction of methanol synthesis [28,43,44]. As well known, there are two important competitive reactions in CO₂ hydrogenation to methanol. The first one is the synthesis of methanol (3) and the second one is the reverse water gas shift (RWGS) reaction (4). As shown in Reaction (3), the synthesis of methanol is an exothermic reversible reaction and its equilibrium constant increased upon declining of reaction temperature. In addition, the methanol synthesis reaction has a lower apparent activation energy compared to RWGS reaction [8,45], which indicates that the increase of methanol relative production is higher than that of CO with decreasing reaction temperature. However, the CH₃OH selectivity for RHT-6 was much lower than those for other catalysts, only around 50%. Some researchers suggested that the monovalent copper species could promote CO production during the RWGS reaction [6,46]. Consequently, the low CH₃OH selectivity for RHT-6 might be attributed to the presence of Cu⁺ species.



According to the reported mechanistic studies, the copper particle size (d_{Cu}) and the exposed copper surface area (S_{Cu}) played an important role for the catalytic performance of copper-based catalysts [14,47,48]. Variations of d_{Cu} and S_{Cu} as a function of the CO₂

conversion for the various Cu/ZnO/Al₂O₃/ZrO₂ catalysts at 463 K are presented in Fig. 8a. It was found that the CO₂ conversion increased linearly with decreasing d_{Cu} , while there seemed no relationship between the CO₂ conversion and S_{Cu} . Although RHT-7 exhibited the highest S_{Cu} , the CO₂ conversion for RHT-7 was lower than those for the catalysts prepared at pH ≥ 8.0, and the CO₂ conversion decreased with the decrease of S_{Cu} for the catalysts via phase-pure HTI precursors, proving that a high Cu surface area was an important but not the only influencing parameter. Natesakhawat et al. [38] suggested that smaller crystallites had larger numbers of open planes, edge/defect sites containing coordinately unsaturated atoms which were typically more reactive than fully coordinated species. Behrens et al. [10] also claimed that high activity for the Cu-based catalyst was generated by the presence of steps at the Cu surface. These results indicated that the catalytic activity for CO₂ hydrogenation at low reaction temperature was mainly depended on the particle size of Cu.

To discern the role of copper particle size in the CO₂ hydrogenation to methanol, we attempted to correlate the turnover frequency (TOF), which represents the number of CO₂-molecule hydrogenated on unit site of exposed copper atom per second (s⁻¹), with the d_{Cu} . Results from Table 3 showed that the TOF value increased with increasing pH until it reached a maximum of 7.34×10^{-3} for RHT-9 and then decreased. As illustrated in Fig. 8b the TOF value declined with increasing d_{Cu} over these catalysts, providing direct evidence that methanol synthesis from CO₂ hydrogenation was structurally sensitive. However, the relationship was not linear, and the TOF for RHT-7 was much lower than that for RHT-11 though the difference between d_{Cu} of these two samples was pretty small, suggesting that the TOF value for CO₂ conversion was not simply dependent on the crystallite size of Cu. Many researchers believed that the synergistic interaction among Cu and ZnO was necessary to ensure high catalytic activity in methanol synthesis from CO₂ hydrogenation [38,39,49–51]. In our case, compared with the catalysts resulting from HTI precursors, the interaction between Cu and ZnO for the catalyst derived from zincian malachite was much weaker from XRD, XPS and HRTEM analysis, leading to decrease the catalytic activity. Therefore, RHT-9 exhibited the best catalytic performance for CO₂ hydrogenation to methanol due to the minimum of copper particle size and the efficient interaction among Cu and ZnO.

Table 3The catalytic performance for methanol synthesis from CO₂ hydrogenation over RHT-n catalysts.

Sample	CO ₂ conversion (%)	Selectivity (C-mol%)		CH ₃ OH yield (gcat ⁻¹ h ⁻¹)	TOF × 10 ³ (s ⁻¹)
		CH ₃ OH	CO		
RHT-6	2.6	49.5	50.5	0.011	2.52
RHT-7	6.9	81.1	18.9	0.055	3.26
RHT-8	8.5	80.6	19.4	0.068	5.26
RHT-9	10.7	81.8	18.2	0.087	7.34
RHT-10	9.0	81.6	18.4	0.074	6.66
RHT-11	7.3	81.3	18.7	0.059	4.96

Reaction conditions: T=463 K, P=5.0 MPa, GHSV=4000 h⁻¹, H₂/CO₂/N₂=73/24/3 (molar ratio).

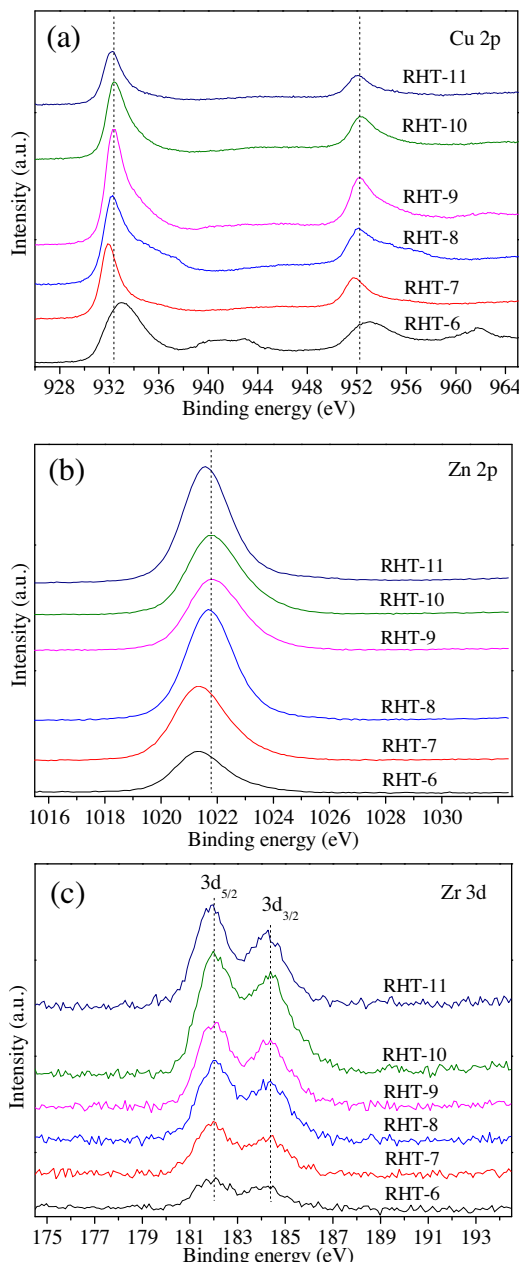


Fig. 6. (a) Cu 2p, (b) Zn 2p and (c) Zr 3d XPS of the reduced RHT-n catalysts.

4. Conclusion

A series of Cu-Zn-Al-Zr precursor materials ($\text{Cu}^{2+}:\text{Zn}^{2+}:\text{Al}^{3+}:\text{Zr}^{4+}=2:1:1.2:0.1$) were prepared by coprecipitation at different pH values (6.0–11.0) and treated under hydrothermal conditions. Zincian malachite was formed as the main phase at the low pH, and both zincian malachite and HTI phases can be detected at pH 8.0. In addition, hydrotalcite alone was selectively produced at the high pH, above 8.0. After calcination and reduction of precursors, Cu/ZnO/Al₂O₃/ZrO₂ catalysts were obtained and tested for CO₂ hydrogenation to methanol at the reaction temperature of 463 K.

Compared with the material resulting from well-crystallized zincian malachite (pH 7.0), the BET specific surface area and Cu surface area for samples derived from phase-pure hydrotalcite-like precursors ($\text{pH} \geq 9.0$) were lower, while smaller Cu particle size and stronger interaction between Cu and ZnO could be obtained. With

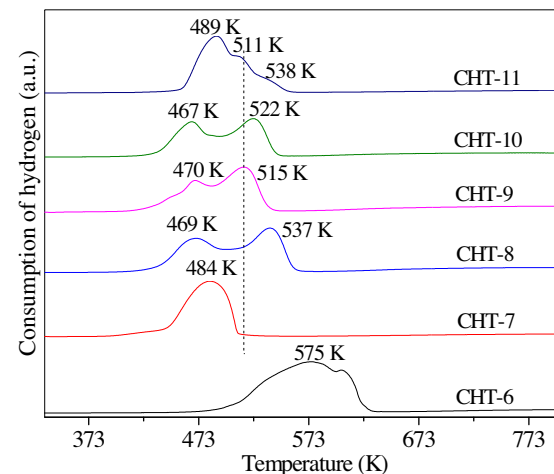
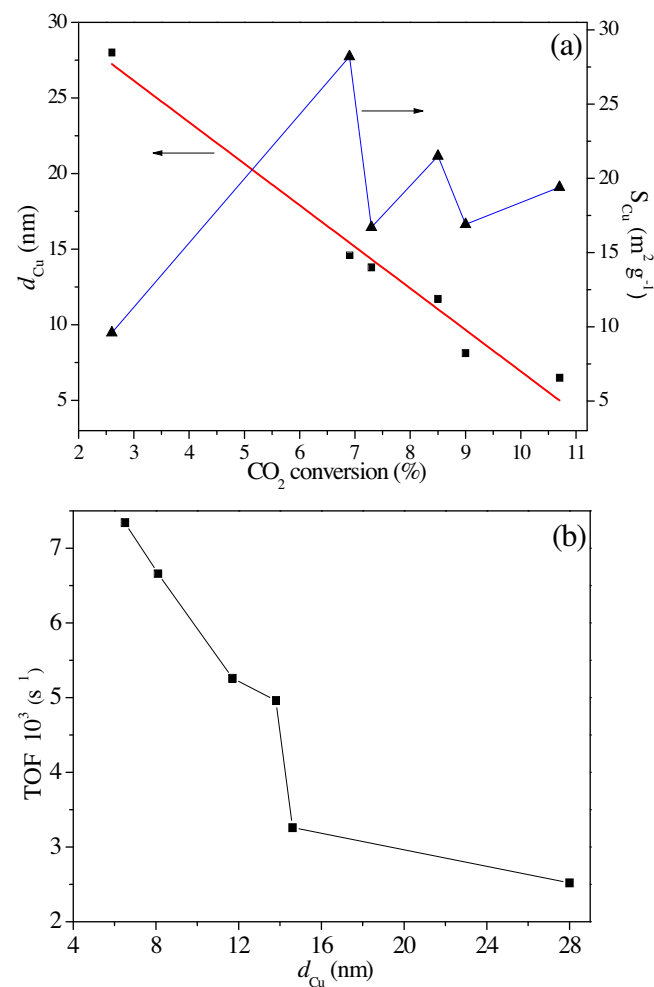


Fig. 7. TPR profiles of the CHT-n samples prepared at various pH conditions.

Fig. 8. (a) Variations of the copper particle size and the exposed copper surface area as a function of CO₂ conversion, and (b) the relationship between the TOF and the copper particle size for the Cu/ZnO/Al₂O₃/ZrO₂ catalysts prepared at various pH conditions. Reaction conditions: $T=463 \text{ K}$, $P=5.0 \text{ MPa}$, GHSV = 4000 h^{-1} , $\text{H}_2/\text{CO}_2/\text{N}_2=73/24/3$ (molar ratio).

increasing pH from 6.0 to 11.0, the Cu particle size first increased until pH 9.0 and then decreased, and both the CO₂ conversion and TOF took the same trend. Additionally, the Cu/ZnO/Al₂O₃/ZrO₂ catalysts via hydrotalcite-like compounds exhibited better

performance compared to the catalysts derived from zincian malachite precursors.

It was also found that the catalytic activity for CO₂ hydrogenation was related to the particle size of Cu and the synergistic interaction among Cu and ZnO. A maximum CH₃OH yield of 0.087 g gcat⁻¹ h⁻¹ with the CO₂ conversion of 10.7% and the CH₃OH selectivity of 81.8% at 463 K and 5.0 MPa was obtained over the Cu/ZnO/Al₂O₃/ZrO₂ catalyst via the phase-pure hydrotalcite-like compound prepared at pH 9.0.

Acknowledgements

This work was financially supported by Strategic Priority Research Program of the Chinese Academy of Sciences (XDA02040602), Shanghai Municipal Science and Technology Commission, China (14DZ1207600, 15ZR1444500), the National Natural Science Foundation of China (21503260), and the Global Innovation Initiative: Increasing the efficiency of CO₂ conversion to liquid fuels (S-ECAGD-13-CA-149 (DT)).

References

- [1] G.A. Olah, A. Geoppert, G.K.S. Prakash, *Beyond Oil and Gas: The Methanol Economy*, first ed., Wiley-VCH, Weinheim, 2006, pp. 173–187, 239–245.
- [2] S. Saeidi, N.A.S. Amin, M.R. Rahimpour, *J. CO₂ Util.* 5 (2014) 66–81.
- [3] Q. Sun, Y.L. Zhang, H.Y. Chen, J.F. Deng, D. Wu, S.Y. Chen, *J. Catal.* 167 (1997) 92–105.
- [4] A. Bansode, A. Urakawa, *J. Catal.* 309 (2014) 66–70.
- [5] L.X. Zhang, Y.C. Zhang, S.Y. Chen, *Appl. Catal. A: Gen.* 415 (2012) 118–123.
- [6] O. Martin, J. Perez-Ramirez, *Catal. Sci. Technol.* 3 (2013) 3343–3352.
- [7] N. Pasupulety, H. Driss, Y.A. Alhamed, A.A. Alzahrani, M.A. Daous, L. Petrov, *Appl. Catal. A: Gen.* 504 (2015) 308–318.
- [8] X.M. Guo, D.S. Mao, G.Z. Lu, S. Wang, G.S. Wu, *J. Catal.* 271 (2010) 178–185.
- [9] Q. Zhang, Y.Z. Zuo, M.H. Han, J.F. Wang, Y. Jin, F. Wei, *Catal. Today* 150 (2010) 55–60.
- [10] M. Behrens, F. Studt, I. Kasatkin, S. Kuhl, M. Havecker, F. Abild-Pedersen, S. Zander, F. Girsdsies, P. Kurr, B.L. Kniep, M. Tovar, R.W. Fischer, J.K. Norskov, R. Schlogl, *Science* 336 (2012) 893–897.
- [11] J. Liu, C.M. Li, F. Wang, S. He, H. Chen, Y.F. Zhao, M. Wei, D.G. Evans, X. Duan, *Catal. Sci. Technol.* 3 (2013) 2627–2633.
- [12] J. Słoczyński, R. Grabowski, P. Olszewski, A. Kozłowska, J. Stoch, M. Lachowska, J. Skrzypek, *Appl. Catal. A: Gen.* 310 (2006) 127–137.
- [13] A. Venugopal, J. Palgunadi, J.K. Deog, O.S. Joo, C.H. Shin, *J. Mol. Catal. A: Chem.* 302 (2009) 20–27.
- [14] P. Gao, F. Li, N. Zhao, F.K. Xiao, W. Wei, L.S. Zhong, Y.H. Sun, *Appl. Catal. A: Gen.* 468 (2013) 442–452.
- [15] E. Frei, A. Schaadt, T. Ludwig, H. Hillebrecht, I. Krossing, *ChemCatChem* 6 (2014) 1721–1730.
- [16] E.B. Batyrev, J.C. van den Heuvel, J. Beckers, W.P.A. Jansen, H.L. Castricum, *J. Catal.* 229 (2005) 136–143.
- [17] C. Baltes, S. Vukovic, F. Schuth, *J. Catal.* 258 (2008) 334–344.
- [18] X.M. Guo, D.S. Mao, S. Wang, G.S. Wu, G.Z. Lu, *Catal. Commun.* 10 (2009) 1661–1664.
- [19] P. Gao, F. Li, H.J. Zhan, N. Zhao, F.K. Xiao, W. Wei, L.S. Zhong, H. Wang, Y.H. Sun, *J. Catal.* 298 (2013) 51–60.
- [20] P. Gao, F. Li, F.K. Xiao, N. Zhao, N.N. Sun, W. Wei, L.S. Zhong, Y.H. Sun, *Catal. Sci. Technol.* 2 (2012) 1447–1454.
- [21] S. Kuhl, A. Tarasov, S. Zander, I. Kasatkin, M. Behrens, *Chem.–Eur. J.* 20 (2014) 3782–3792.
- [22] S. Kuhl, J. Schumann, I. Kasatkin, M. Havecker, R. Schlogl, M. Behrens, *Catal. Today* 246 (2015) 92–100.
- [23] G. Busca, U. Costantino, F. Marmottini, T. Montanari, P. Patrono, F. Pinzari, G. Ramis, *Appl. Catal. A: Gen.* 310 (2006) 70–78.
- [24] L.H. Zhang, C. Zheng, F. Li, D.G. Evans, X. Duan, *J. Mater. Sci.* 43 (2008) 237–243.
- [25] H. Wang, P. Gao, T.J. Zhao, W. Wei, Y.H. Sun, *Sci. China Chem.* 58 (2015) 79–92.
- [26] S. He, Z. An, M. Wei, D.G. Evans, X. Duan, *Chem. Commun.* 49 (2013) 5912–5920.
- [27] P. Gao, F. Li, F.K. Xiao, N. Zhao, W. Wei, L.S. Zhong, Y.H. Sun, *Catal. Today* 194 (2012) 9–15.
- [28] P. Gao, R.Y. Xie, H. Wang, L.S. Zhong, L. Xia, Z.Z. Zhang, W. Wei, Y.H. Sun, *J. CO₂ Util.* 11 (2015) 41–48.
- [29] F. Kovanda, T. Rojka, P. Bezdicka, K. Jiratova, L. Obalova, K. Pacultova, Z. Bastl, T. Grygar, *J. Solid State Chem.* 182 (2009) 27–36.
- [30] F.B. Saiah, B.L. Su, N. Bettahar, J. Hazard. Mater. 165 (2009) 206–217.
- [31] S.K. Sharma, P.K. Kushwaha, V.K. Srivastava, S.D. Bhatt, R.V. Jasra, *Ind. Eng. Chem. Res.* 46 (2007) 4856–4865.
- [32] M. Behrens, *J. Catal.* 267 (2009) 24–29.
- [33] C. Li, X. Yuan, K. Fujimoto, *Appl. Catal. A: Gen.* 469 (2014) 306–311.
- [34] J. Cheng, X.P. Wang, J.J. Yu, Z.P. Hao, Z.P. Xu, *J. Phys. Chem. C* 115 (2011) 6651–6660.
- [35] D. Qiao, C.L. Xu, J. Xu, *Catal. Commun.* 45 (2014) 44–48.
- [36] M. Behrens, I. Kasatkin, S. Kuhl, G. Weinberg, *Chem. Mater.* 22 (2010) 386–397.
- [37] I.U. Din, M.S. Shaharun, D. Subbarao, A. Naeem, *J. Power Sources* 274 (2015) 619–628.
- [38] S. Natesakhawat, J.W. Lekse, J.P. Baltrus, P.R. Ohodnicki, B.H. Howard, X.Y. Deng, C. Matranga, *ACS Catal.* 2 (2012) 1667–1676.
- [39] P. Gao, L.S. Zhong, L.N. Zhang, H. Wang, N. Zhao, W. Wei, Y.H. Sun, *Catal. Sci. Technol.* 5 (2015) 4365–4377.
- [40] C. Tisseraud, C. Comminges, T. Belin, H. Ahouari, A. Soualah, Y. Pouilloux, A. Le Valant, *J. Catal.* 330 (2015) 533–544.
- [41] F. Arena, G. Mezzatesta, G. Zafarana, G. Trunfio, F. Frusteri, L. Spadaro, *J. Catal.* 300 (2013) 141–151.
- [42] R. Ladera, F.J. Perez-Alonso, J.M. Gonzalez-Carballo, M. Ojeda, S. Rojas, J.L.G. Fierro, *Appl. Catal. B: Environ.* 142 (2013) 241–248.
- [43] P. Gao, F. Li, L.N. Zhang, N. Zhao, F.K. Xiao, W. Wei, L.S. Zhong, Y.H. Sun, *J. CO₂ Util.* 2 (2013) 16–23.
- [44] H. Ban, C. Li, K. Asami, K. Fujimoto, *Catal. Commun.* 54 (2014) 50–54.
- [45] A. Bansode, B. Tidona, P.R. von Rohr, A. Urakawa, *Catal. Sci. Technol.* 3 (2013) 767–778.
- [46] C.S. Chen, W.H. Cheng, S.S. Lin, *Appl. Catal. A: Gen.* 238 (2003) 55–67.
- [47] A. Karelovic, P. Ruiz, *Catal. Sci. Technol.* 5 (2015) 869–881.
- [48] L. Li, D.S. Mao, J. Yu, X.M. Guo, *J. Power Sources* 279 (2015) 394–404.
- [49] G. Bonura, M. Cordaro, C. Cannilla, F. Arena, F. Frusteri, *Appl. Catal. B: Environ.* 152 (2014) 152–161.
- [50] P. Gao, F. Li, H.J. Zhan, N. Zhao, F.K. Xiao, W. Wei, L.S. Zhong, Y.H. Sun, *Catal. Commun.* 50 (2014) 78–82.
- [51] W.J. Cai, P.R. de la Piscina, J. Toyir, N. Homs, *Catal. Today* 242 (2015) 193–199.